Research
A SCIENCE PARTNER JOURNAL

RESEARCH ARTICLE

Superconducting, Topological, and Transport Properties of Kagome Metals $CsTi_3Bi_5$ and $RbTi_3Bi_5$

Xin-Wei Yi[1], Zheng-Wei Liao[1], Jing-Yang You[2*], Bo Gu[1,3*], and Gang Su[1,3*]

[1]School of Physical Sciences, University of Chinese Academy of Sciences, Beijing 100049, China. [2]Department of Physics, Faculty of Science, National University of Singapore, 117551, Singapore. [3]Kavli Institute for Theoretical Sciences, and CAS Center for Excellence in Topological Quantum Computation, University of Chinese Academy of Sciences, Beijing 100190, China.

*Address correspondence to: phyjyy@nus.edu.sg (J-Y.Y.); gubo@ucas.ac.cn (B.G.); gsu@ucas.ac.cn (G.S.)

Citation: Yi XW, Liao ZW, You JY, Gu B, Su G. Superconducting, Topological, and Transport Properties of Kagome Metals $CsTi_3Bi_5$ and $RbTi_3Bi_5$. *Research* 2023;6:Article 0238. https://doi.org/10.34133/research.0238

Submitted 7 July 2023
Accepted 5 September 2023
Published 2 October 2023

Copyright © 2023 Xin-Wei Yi et al. Exclusive licensee Science and Technology Review Publishing House. No claim to original U.S. Government Works. Distributed under a Creative Commons Attribution License 4.0 (CC BY 4.0).

The recently discovered ATi_3Bi_5 (A=Cs, Rb) exhibit intriguing quantum phenomena including superconductivity, electronic nematicity, and abundant topological states. ATi_3Bi_5 present promising platforms for studying kagome superconductivity, band topology, and charge orders in parallel with AV_3Sb_5. In this work, we comprehensively analyze various properties of ATi_3Bi_5 covering superconductivity under pressure and doping, band topology under pressure, thermal conductivity, heat capacity, electrical resistance, and spin Hall conductivity (SHC) using first-principles calculations. Calculated superconducting transition temperature (T_c) of $CsTi_3Bi_5$ and $RbTi_3Bi_5$ at ambient pressure are about 1.85 and 1.92 K. When subject to pressure, T_c of $CsTi_3Bi_5$ exhibits a special valley and dome shape, which arises from quasi-two-dimensional compression to three-dimensional isotropic compression within the context of an overall decreasing trend. Furthermore, T_c of $RbTi_3Bi_5$ can be effectively enhanced up to 3.09 K by tuning the kagome van Hove singularities (VHSs) and flat band through doping. Pressures can also induce abundant topological surface states at the Fermi energy (E_F) and tune VHSs across E_F. Additionally, our transport calculations are in excellent agreement with recent experiments, confirming the absence of charge density wave. Notably, SHC of $CsTi_3Bi_5$ can reach up to $226\hbar \cdot (e \cdot \Omega \cdot cm)^{-1}$ at E_F. Our work provides a timely and detailed analysis of the rich physical properties for ATi_3Bi_5, offering valuable insights for further experimental verifications and investigations in this field.

Introduction

The kagome lattice composed of tiled corner-sharing triangles is a well-known two-dimensional (2D) prototype lattice, in which topological magnetism, superconductivity, and frustration have been extensively studied in recent decades [1,2]. The ideal electronic band structure of kagome lattice is characterized by flat bands, Dirac cones, quadratic band touching points, and van Hove singularities (VHSs) (Fig. S1B). The flat bands originating from the destructive interference of wave functions suggest a strong correlation between electrons and can induce special negative magnetism [3], fractional quantum Hall effect [4,5], Wigner crystallization [6], high-temperature superconductivity [7], etc. Moreover, the spin-orbit coupling (SOC) at the massless Dirac points and quadratic band touching points introduces energy gaps, which can give rise to nontrivial Z_2 topology akin to topological insulators. These gaps can even exhibit Chern gaps when subjected to magnetization [8,9]. Fermi surface instabilities due to sublattice interference near VHS may cause different long-range charge orders and unconventional superconductivity [10–12]. Additionally, other novel physical properties, including Wely points [13–15], giant anomalous Hall effect [16–18], quantum anomalous Hall effect [19,20], and topological superconductors [21,22], are all intriguing research topics of kagome structure.

The recently discovered AV_3Sb_5 (A=K, Rb, Cs) kagome family exhibits various attractive properties [23]. As the pioneering examples of quasi-2D kagome superconductors, their superconducting transition temperatures (T_c) are about 1.8 to 2.5 K under ambient pressure [24–27]. Alongside the emergence of 2×2 charge density wave (CDW) induced by VHSs with transition temperatures of about 100 K [28–30], AV_3Sb_5 hosts a variety of unconventional charge orders, including a nematic phase reminiscent of iron-based superconductors [31,32], a pair density wave similar to copper-based superconductors [27], and a 4×1 CDW that induces striking phase fluctuation [33,34]. Pressure and doping are two effective ways to manipulate the phase diagram of AV_3Sb_5. Multiple superconductivity domes simultaneously emerge intertwined with several CDW orders under pressure [30,32,35,36]. Experimental substitution doping with Ti, Nb, Ta, Mo, Mn, Cr, Sn, and As in AV_3Sb_5 has been achieved, providing control over superconductivity, CDW, and nematicity [37–46]. CsV_3Sb_5, in particular, possesses both abundant nontrivial Z_2 topological surface states (TSS) and superconductivity [25,47] and has been instrumental in resolving possible Majorana zero modes within vortex cores [48].

High-throughput density functional theory calculations have been employed to analyze a range of compounds based on the AV_3Sb_5 prototype structure, revealing 24 dynamically stable compounds with superconductivity, abundant TSS and CDW [49]. Among them, ATi_3Bi_5 (A=Rb, Cs) compounds with enhanced T_c of about 4.8 K and electronic nematicity have recently been synthesized [50–53]. Another kagome superconductor family, similar to ATi_3Bi_5, has also been predicted and awaits experimental verification [54]. The nematic order in CsV_3Sb_5 is considered as the vestige order of CDW [31]. However, the original lattice structure of ATi_3Bi_5 has been confirmed to be highly stable and devoid of CDW, as supported by calculations and thermal transport measurements [49–51,55]. The presence of orbital-selective nematic order and intertwined superconductivity in ATi_3Bi_5 provides a new platform for exploring the multiorbital correlation effect in nematic superconductors. In addition, exotic electronic structures have been observed in ATi_3Bi_5 using angle-resolved photoemission spectroscopy, including flat band, type II and type III Dirac nodal lines and Z_2 TSS [56–61]. These fascinating properties make ATi_3Bi_5 ideal systems for investigating various kagome-related physics with reference to AV_3Sb_5. Consequently, further investigations are imperative, particularly in examining the effects of pressure and doping on the properties of superconductivity and topology.

In this paper, we analyze the superconducting and topological properties of ATi_3Bi_5 under pressure and doping by first-principles calculations. Estimated T_c's of $CsTi_3Bi_5$ and $RbTi_3Bi_5$ at ambient pressure are about 1.85 and 1.92 K. We observe the emergence of a special valley and dome in the T_c of $CsTi_3Bi_5$ under pressure, which is due to the transition from quasi-2D compression to three-dimensional (3D) isotropic compression within the range of 10 to 20 GPa, accompanied by a decreased background effect across all pressure ranges. Moreover, electron–phonon coupling (EPC) calculations with both a rigid band model and atomic substitution doping confirm the substantial enhancement of superconductivity in $RbTi_3Bi_5$ under doping. Additionally, pressure can lead to the presence of abundant TSS near E_F. We also discuss properties such as thermal conductivity, heat capacity, and electrical resistance, which are consistent with recent experimental findings, indicating the absence of CDW. We find that $CsTi_3Bi_5$ exhibits an intrinsic spin Hall conductivity (SHC) of up to $226\hbar \cdot (e \cdot \Omega \cdot cm)^{-1}$ at the Fermi energy (E_F). Our findings indicate that both doping and pressure prove to be effective means of tuning the electronic band structures and superconductivity of kagome ATi_3Bi_5.

Results and Discussion

Electronic structure of $CsTi_3Bi_5$

The ATi_3Bi_5 compounds exhibit a layered structure with the space group P6/mmm (No. 191) as illustrated in Fig. 1A. The central Ti_3Bi layer consists of a Ti-kagome net intertwined with a Bi triangular net, sandwiched between two Bi honeycomb layers. The triangular layers composed of A atoms are loosely bonded with the central Ti–Bi sheets. Bi atoms occupy two distinct Wyckoff positions, designated as Bi1 and Bi2, respectively. The calculated electronic band structures and partial electronic density of states (DOS) with SOC for $CsTi_3Bi_5$ are plotted in Fig. 1B. By assigning colors to the bands based on the weights of different Ti atomic orbitals, we can identify a clear kagome flat band at about −0.4eV, VHSs at M and L points (namely, VHS1 and VHS2) at about 0.2 eV and massive Dirac points at

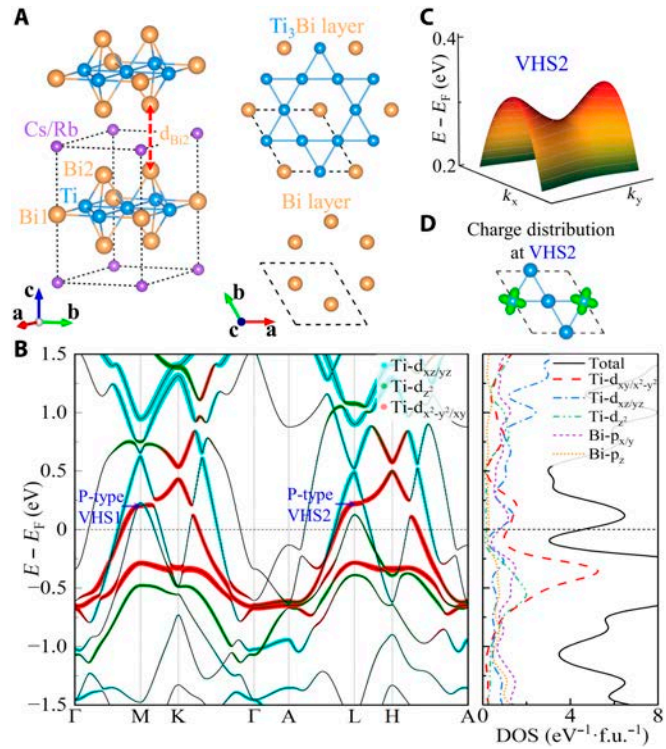


Fig. 1. The crystal structure and electronic band structure of $CsTi_3Bi_5$. (A) The side view of crystal structure and top views of Ti_3Bi kagome layer and Bi hexagonal layer. "d_{Bi2}" represents the vertical distance between Bi2 atoms in the adjacent primitive lattices, indicated by the black dotted lines. (B) Calculated electronic band structure projected by different orbitals of Ti atoms and partial DOS with SOC for $CsTi_3Bi_5$. Two kagome VHSs near the Fermi level are labeled as "VHS1" and "VHS2", respectively. (C) 3D band structure near VHS2, with gray curves indicating constant energy contours. (D) Charge density distribution of the electronic state at VHS2 (isovalue: 0.003 e/bohr^3).

K and H points contributed by Ti-$d_{x^2-y^2/xy}$ orbitals. The VHSs and flat band of Ti-$d_{x^2-y^2/xy}$ orbitals give rise to two DOS peaks at the corresponding energy levels. Notably, clear saddle features are observed in the 3D band structure near VHS2 as plotted in Fig. 1C.

Two distinct VHSs arise from the general kagome electronic bands, namely, p-type and m-type VHSs, corresponding to pure and mixed sublattice characteristics at the VHS, respectively. The charge density distribution of the electronic state at the VHS2 shows pronounced in-plane d-orbital features and a p-type character as illustrated in Fig. 1D. Unlike CsV_3Sb_5, where all p-type VHSs are located above corresponding Dirac points, the p-type VHS1 and VHS2 of $CsTi_3Bi_5$ lie below Dirac points in Fig. 1B. To clarify this, we construct a tight-binding kagome model with a single orbital on each sublattice and nearest-neighboring (NN) hopping, a three-band Hamiltonian can be written as follows,

$$H = \sum_{\substack{i,j \\ i \neq j}} 2t\cos\left(k \cdot d_{ij}\right) c_{i,k}^{\dagger} c_{j,k}, \ (i,j = A,B,C) \qquad (1)$$

where t, d_{ij}, and $k = (k_x, k_y, k_z)$ represent the NN hopping parameter, NN space vector of sublattice i and j, and wavevector of reciprocal space, respectively. A, B, and C represent three kagome sublattices. This toy kagome model produces the flat band spanning the entire Brillouin zone, VHSs at $\overline{M}$, Dirac point at $\overline{K}$,

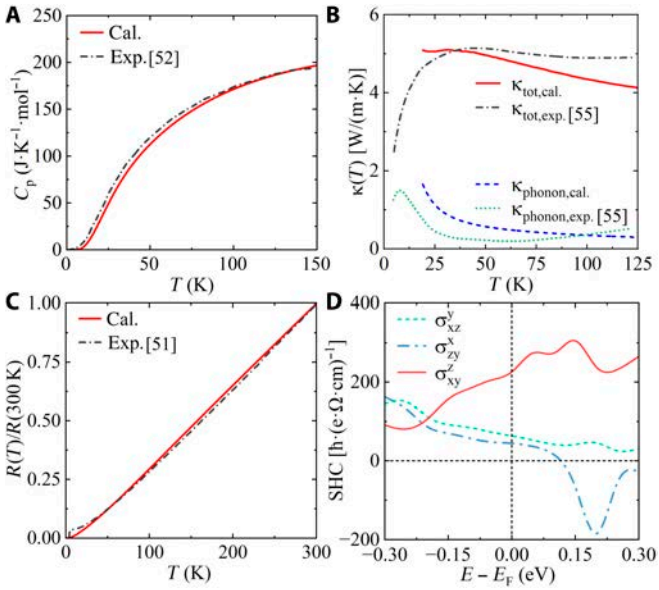


Fig. 2. Heat capacity and transport properties of $CsTi_3Bi_5$. Calculated temperature dependences of (A) heat capacity, (B) longitudinal thermal conductivity, and (C) longitudinal electrical resistivity, compared with experimentals [51,52,55]. (D) Calculated three independent components of SHC tensor as a function of the chemical potential.

and quadratic band touching point at $\bar{\Gamma}$ as shown in Fig. S1B of the supplemental information. By adjusting t, it becomes apparent that for $t > 0$, the p-type and m-type VHSs are located above and below the Dirac points, respectively, and the flat band resides at the top of band structure. Conversely, for $t < 0$, the bands are reversed. This observation indicates that in the kagome sublattice of CsV_3Sb_5, all the relevant NN hopping parameters are positive, while for the Ti-$d_{x^2-y^2/xy}$ orbitals in $CsTi_3Bi_5$, the NN hopping parameters exhibit negative values. P-type VHSs can induce Fermi surface instabilities [10–12], and further investigations are warranted to explore their connection with the nematic and superconducting properties in $CsTi_3Bi_5$.

Transport properties of $CsTi_3Bi_5$

To give a reference for the transport properties of ATi_3Bi_5, we calculate the temperature dependence of heat capacity C_p, thermal conductivity κ, and resistance R for $CsTi_3Bi_5$. These results are compared with recent experimental data as plotted in Fig. 2A to C. Part of the calculated results for $RbTi_3Bi_5$ are listed in Fig. S3. Overall, our transport calculations are in quantitative agreement with the experimental findings, demonstrating the reliability of our calculations. Obviously, there are no phase transition signatures in any of the transported quantities, suggesting the absence of CDW. In contrast to CsV_3Sb_5, the total thermal conductivity $\kappa_{tot,cal}$ of $CsTi_3Bi_5$ is primarily governed by electronic contributions rather than phonon thermal conductivity $\kappa_{phonon,cal}$ [55]. We choose the results with the highest residual resistance ratios from [51], where the impurity concentration is the lowest in that experiment. The resistance of $CsTi_3Bi_5$, as shown in Fig. S3B, is much smaller than that of AV_3Sb_5 [25]. The calculated $R(T)/R(300\ K)$ values align well with the experimental results at high temperatures but underestimate the experimental data below 30 K as shown in Fig. 2C. This discrepancy arises that our resistance calculations solely consider the electron–phonon interaction and do not account for electron–electron interactions. In the experimental resistance–temperature behavior, a quadratic dependence below 30 K and a linear dependence above 50 K can be observed, corresponding to electron–electron and electron–phonon interactions in the normal metal, respectively. It is important to note that our calculations of the transport properties are performed on the normal phase of $CsTi_3Bi_5$ and not the superconducting phase. Therefore, our calculations do not capture the information regarding the superconducting phase transition.

In addition to the aforementioned transport properties, we also calculate the three independent components of SHC tensor, i.e., σ^z_{xy}, σ^x_{zy}, and σ^y_{xz}, as a function of the chemical potential for $CsTi_3Bi_5$ in Fig.2D. The magnitudes of three components can reach up to $226\hbar \cdot (e \cdot \Omega \cdot cm)^{-1}$ at E_F. The large SHC comes from a narrow band gap opened by large SOC [62]. The large SHC observed in $CsTi_3Bi_5$ holds great potential for applications in spintronic devices.

Superconductivity of $CsTi_3Bi_5$ under pressure

The superconducting T_c of CsV_3Sb_5 at pressures above 2 GPa, in the absence of CDW, have been found to be in good agreement between EPC calculations and experimental results [63,64]. Therefore, we can also expect density functional theory calculations to accurately capture the true superconductivity in ATi_3Bi_5. The estimated T_c's of $CsTi_3Bi_5$ and $RbTi_3Bi_5$ at ambient pressure are about 1.85 and 1.92 K, respectively. The superconducting properties of both materials share remarkable similarities, so we select $CsTi_3Bi_5$ for a detailed analysis of superconductivity under pressure.

In previous reports on AV_3Sb_5 (A = K, Rb, Cs) pressurized experiments, the upper pressure limit was typically applied below 50 GPa [28,30,32,35,36,65]. Our calculation results show that some physical quantities related to superconductivity change monotonically with pressure above 20 GPa. Thus, we choose the pressure range of 0 to 50 GPa to investigate superconducting properties in the main text. The additional results at the pressure of 50 to 150 GPa can be found in Fig. S4. Our calculated T_c and EPC constant λ as a function of pressure are shown in Fig. 3A. Both parameters decrease in the ranges of 0 to 10 and 20 to 50 GPa, while they increase within the range of 10 to 20 GPa, forming a unique valley and dome shape under pressure. The corresponding logarithmic average of the phonon frequency ω_{log} and the electronic DOS at the Fermi energy $N(E_F)$ are shown in Fig. 3B. $N(E_F)$ shows an almost linear decrease with increasing pressure, while ω_{log} exhibits an overall increase but with a decreasing trend specifically within the 10 to 20 GPa. It is noted that T_c is explicitly proportional to ω_{log} as described by McMillan semi-empirical formula [66,67], $T_c = \frac{\omega_{log}}{1.2}\exp\left[-\frac{1.04(1+\lambda)}{\lambda-\mu^*(1+0.62\lambda)}\right]$, whereas the variation of T_c in $CsTi_3Bi_5$ shows an opposite trend compared with ω_{log} in Fig. 3A and B. To address this apparent contradiction, we differentiate McMillan formula with respect to pressure value (P), which gives

$$\frac{dT_c}{dP} = T_c \cdot \left[\frac{\partial \ln \omega_{\log}}{\partial P} + \Delta \cdot \frac{\partial \lambda}{\partial P}\right], \quad (2)$$

$$\text{and} \quad \Delta = \frac{1.04(1+0.38\mu^*)}{[\lambda-\mu^*(1+0.62\lambda)]^2}.$$

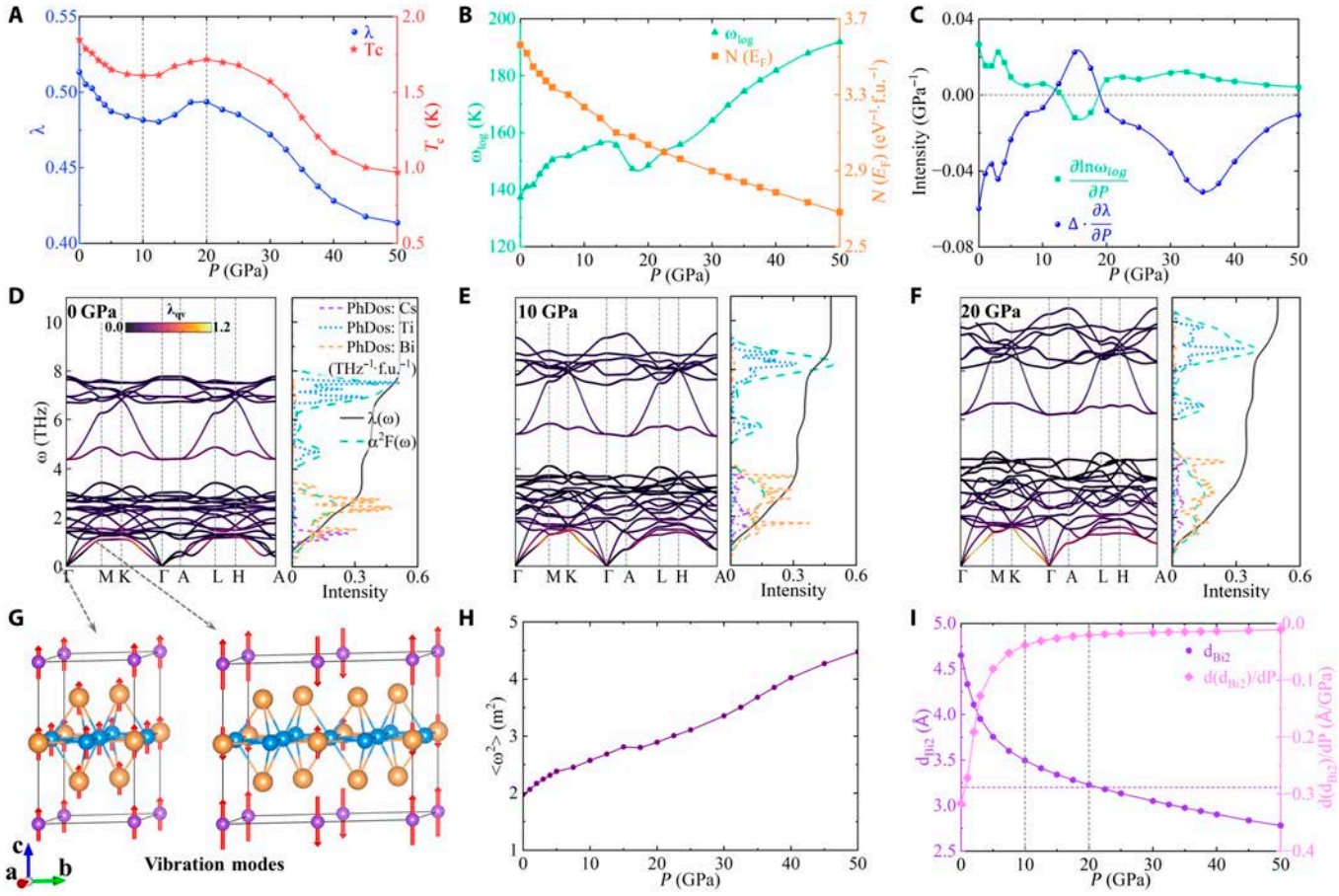


Fig. 3. Superconducting properties of $CsTi_3Bi_5$ under pressure in the range of 0 to 50 GPa. (A) Superconducting transition temperature T_c and EPC λ under pressure. (B) Logarithmic average frequency ω_{log}(K) and electronic DOS per formula unit (f.u.) at the Fermi energy $N(E_F)$ under pressure. (C) $\frac{\partial \ln \omega_{log}}{\partial P}$ and $\Delta \cdot \frac{\partial \lambda}{\partial P}$ under pressure. Phonon spectra colored by EPC strength $\lambda_{q\nu}$, projected phDOS, Eliashberg spectral function $\alpha^2F(\omega)$, and cumulative frequency-dependent EPC $\lambda(\omega)$ at (D) 0, (E) 10, and (F) 20 GPa, respectively. (G) Vibration modes at the lowest acoustic branch near Γ and M points, which both are contributed by the vibrations along the c axis. (H) The average of square of phonon frequency $\langle \omega^2 \rangle$ under pressure. (I) d_{Bi2} denoted in Fig. 1A and $d(d_{Bi2})/dP$ under pressure. The horizontal dashed line indicates the Bi atomic diameter of 3.2Å.

We calculate two terms in the brackets separately and illustrate them in Fig. 3C. It becomes evident that λ and ω_{log} make totally opposite contributions to $\frac{dT_c}{dP}$ across all pressure ranges. However, $\frac{\partial \ln \omega_{log}}{\partial P}$ is much smaller than $\Delta \cdot \frac{\partial \lambda}{\partial P}$. This observation explains the reason why T_c follows the same trend as λ but not ω_{log} under pressure.

The remaining question is why λ (T_c) displays a unique valley and dome shape under pressure. To shed light on this, we present the phonon spectra, projected phonon DOS (phDOS), Eliashberg spectral function $\alpha^2F(\omega)$, and cumulative frequency-dependent EPC $\lambda(\omega)$ in Fig. 3D to F. The corresponding results for other pressures can be found in Fig. S5. As pressure increases, the phonon frequencies (ω) within the phonon spectra noticeably increase, which is a common characteristic observed in many materials. This makes the average of the square of phonon frequency $\langle \omega^2 \rangle$ almost linearly increase under pressure as seen in Fig. 3H. From the definition of λ, we have $\lambda = \frac{N(E_F)\langle I^2 \rangle}{M\langle \omega^2 \rangle}$ and $\langle \omega^2 \rangle = \left[\frac{2}{\lambda}\int_0^\infty \alpha^2F(\omega)\omega d\omega\right]$, where $\langle I^2 \rangle$ is the mean-square electron-ion matrix element, and M is the ionic mass. It is clear that λ is proportional to $N(E_F)$ and inversely proportional to $\langle \omega^2 \rangle$. The combination of $N(E_F)$ and $\langle \omega^2 \rangle$ results in an overall decrease in λ. This mechanism accounts for the downward trend of λ and T_c within the range of 0 to 10 and 20 to 50 GPa.

Upon conducting a more detailed analysis of the phonon spectra and phDOS, we can find that the phonon spectra under pressure can be well separated into distinct high- and low-frequency regions. Specifically, the high-frequency region is mainly contributed by kagome Ti atoms, displaying clear kagome phonon flat band and VHSs. On the other hand, the low-frequency region primarily corresponds to the vibrational modes of Cs and Bi atoms. By separating λ into two components, namely, λ_{Cs+Bi} and λ_{Ti}, we observe that λ_{Ti} gradually decreases with increasing pressure due to the aforementioned background effect, while λ_{Cs+Bi} exhibits exactly the same trend as λ, as seen in Fig. S6A. Consequently, our analysis focuses on examining the low-frequency region within the phonon spectra in order to elucidate the trend of λ.

The total EPC λ can be decomposed into the average coupling strengths $\lambda_{q\nu}$ over the Brillouin zone with $\lambda = \sum_{q,\nu} \lambda_{q\nu}$. By coloring the phonon spectra with $\lambda_{q\nu}$, we find that the high $\lambda_{q\nu}$ are mainly concentrated in the lowest acoustic branch. Taking vibration modes of the lowest acoustic branch near Γ and M point as examples in Fig. 3G, we observe that these modes primarily involve vibrations along the c axis. Thus, based

on our calculations, we can infer that the anomalous increase of λ within 10 to 20 GPa originates from the contributions of $\lambda_{q\nu}$ associated with the out-of-plane atomic vibrations.

Next, we analyze superconductivity under pressure from a structural perspective. The vertical distance between Bi2 atoms in adjacent Ti_3Bi_5 sheets is defined as d_{Bi2} as illustrated in Fig. 1A. Because of the quasi-2D structural features of $CsTi_3Bi_5$, d_{Bi2} is quite large, and interlayer interactions are weak. At low pressures, $d(d_{Bi2})/dP$ exhibits large values and changes dramatically. However, as the pressure exceeds 10 GPa, the rate of change in d_{Bi2} starts to slow down. Furthermore, when $P > 20$ GPa, it approaches a nearly constant value. This trend is also reflected in the ratio of the out-of-plane and in-of-plane lattice parameters c/a as depicted in Fig. S6B. At 20 GPa, d_{Bi2} becomes approximately equal to the Bi atomic diameter of 3.2Å, indicating the formation of covalent bonds among the Bi2 atoms around this pressure. These results demonstrate that the structure undergoes a quasi-2D compression below 10 GPa. The weak coupling between Cs atoms and Ti_3Bi_5 sheets leads to a pronounced response of the out-of-plane lattice parameter c to applied pressure. At 10 GPa, the Bi atoms of neighboring Ti_3Bi_5 sheets start to interact, leading to a dramatic enhancement of $\lambda_{q\nu}$ associated with out-of-plane vibrations. However, as the pressure exceeds 20 GPa, the structure exhibits a 3D isotropic compression characteristic. The interaction between Bi2 atoms no longer increases but gradually decreases due to the underlying background effect mentioned earlier.

Topological states of $CsTi_3Bi_5$ under pressure

Next, we explore the effect of pressure on electronic structures. We illustrate the calculation results at pressures of 5, 25, and 40 GPa in Fig. 4A to C, which depict the electronic band structures of $CsTi_3Bi_5$ with SOC. The increased interlayer interaction under pressure profoundly impacts the band structures, leading to notable changes in the energy levels of VHSs and flat band, particularly at higher pressures. With increasing pressure, both VHSs and flat band gradually shift downwards. Remarkably, the VHSs progressively approach the vicinity of the Fermi level under pressure. Exploring the potential nematicity and other phases induced by VHSs through pressure engineering holds substantial interest.

The nontrivial TSS near Γ point of $CsTi_3Bi_5$ have been experimentally detected [51,57,58]. However, these TSS are approximately 0.8 eV below the Fermi level, limiting their substantial effects on transport and other related properties. By examining the surface-state spectra of $CsTi_3Bi_5$ under pressure in Fig. 4D to F, we observe the emergence of multiple TSS at time-reversal invariant momenta $\overline{M}$ and $\overline{\Gamma}$, many of which are located in proximity to the Fermi level. Under pressure, these TSS undergo slight energy shifts. Importantly, once these TSSs emerge at a specific pressure, further increases in pressure do not eliminate them. The TSS in $CsTi_3Bi_5$ exhibits high tunability and sensitivity to pressure, primarily due to the dramatic changes in electronic structures.

Superconductivity of $RbTi_3Bi_5$ under doping

$RbTi_3Bi_3$ has similar electronic structure and phonon spectrum to $CsTi_3Bi_3$ as shown in Fig. S7. Therefore, we can expect $RbTi_3Bi_3$ and $CsTi_3Bi_3$ to exhibit similar topological, transport, and superconducting properties. As a result, we do not replicate the calculations performed above for $RbTi_3Bi_5$. Since the T_c of $RbTi_3Bi_5$ is slightly higher than that of $CsTi_3Bi_5$ in our

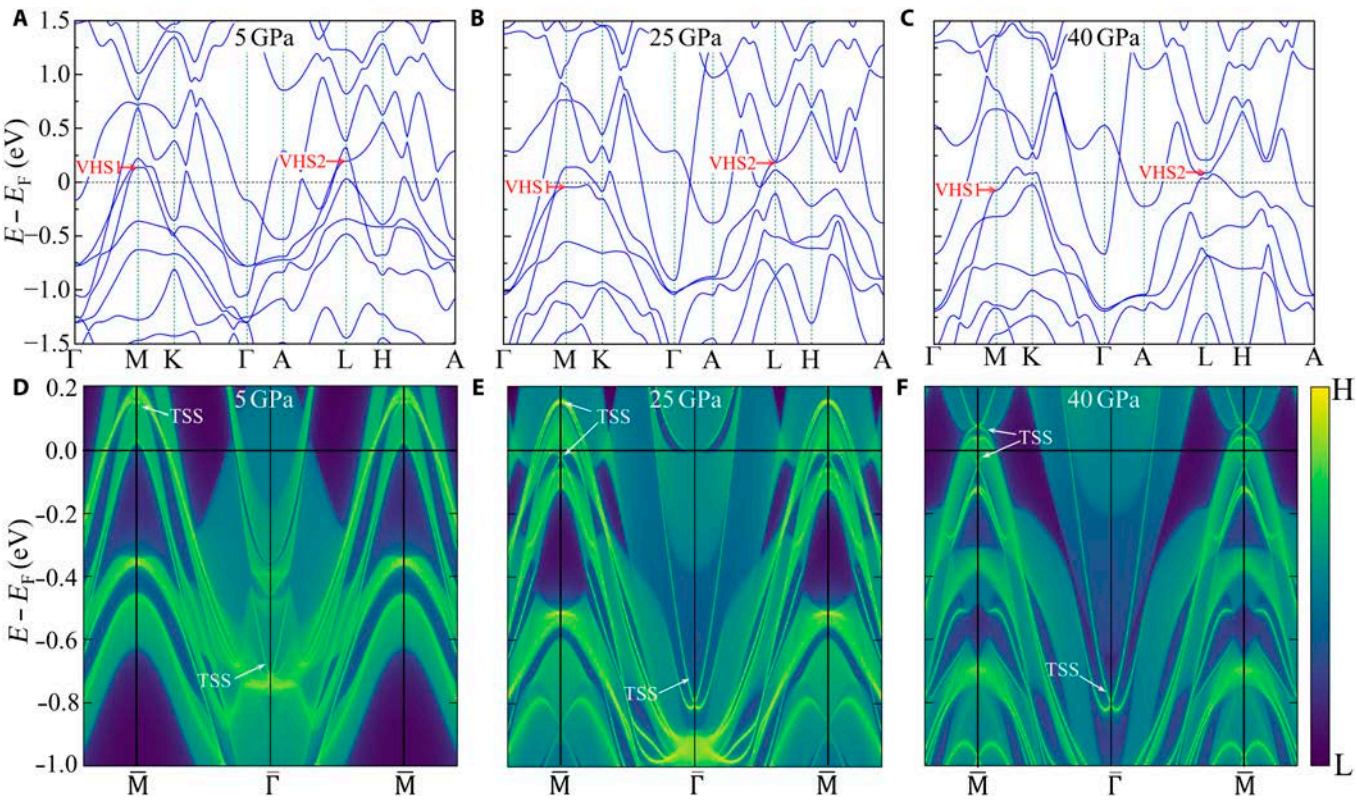


Fig. 4. Electronic band structures and surface-state spectra under pressure for $CsTi_3Bi_5$. Electronic band structures with SOC at (A) 5, (B) 25, and (C) 40 GPa. Surface-state spectra along $\overline{M} - \overline{\Gamma} - \overline{M}$ paths on the (001) plane at (D) 5, (E) 25, and (F) 40 GPa. TSS are indicated with white arrows.

calculations, in this section, we focus on a comprehensive investigation of superconductivity under doping using $RbTi_3Bi_5$.

Doping is an effective method to tune electronic structures and superconductivity. Extensive studies have successfully achieved doping in AV_3Sb_5 to manipulate the competition between superconductivity, CDW, and nematicity [37–46]. Notably, the concentration of Sb replacement doping with Sn in AV_3Sb_5 can reach up to 30% [40]. With reference to AV_3Sb_5, doping in ATi_3Bi_5 is highly feasible. We first employ a rigid band model to analyze the effect of electron and hole doping on superconductivity. Figure 5A illustrates the relative changes in λ, T_c, and $N(E_F)$ under doping. Both electron and hole doping result in enhancements of $N(E_F)$ due to the movement of VHSs and flat band toward the Fermi level. As a consequence, there are dramatic improvements in λ and T_c. Especially under hole doping, the highest $N(E_F)$ can be increased by nearly 2.5 times, and T_c can be increased by nearly 5 times.

In addition to the rigid band model, we also explore specific element substitution doping. Alkali metal substitutions of ATi_3Sb_5, including $LiTi_3Bi_5$, $NaTi_3Bi_5$, and KTi_3Bi_5, are found to be unstable according to our previous study [49]. Instead, we substitute one Ti or Bi atom in each unit cell of ATi_3Bi_5, corresponding to 33% Ti or 20% Bi substitution. Ti is replaced by its neighboring elements (Sc, V, Y, Zr, and Nb), while Bi is substituted by Ga, Sn, Sb, Te, Pb, and Bi. As illustrated in Fig. 1A, the Bi atoms occupy two Wyckoff positions that need to be distinguished. Taking Te doping as an example, we denote the substitution of Bi2 as $RbTi_3TeBi_4$, and the substitution of Bi1 as $RbTi_3Bi_4Te$ as shown in Fig. S8A. For all doped structures, we first carry out fully geometric relaxation and self-consistent iterations in nonmagnetic, ferromagnetic, and antiferromagnetic configurations as seen in Fig. S8B and C. The energies of the three magnetic configurations of all structures are listed in Table S1, which determines the ground state magnetic configuration. Among the doped structures with Bi substitution, the energy of the replacement of Bi2 is consistently higher than that of Bi1. This suggests that the impurity prefers to substitute the Wyckoff position of Bi1. In addition, Sc-, Y-, and Ga-doped $CsTi_3Bi_5$ and $RbTi_3Bi_5$ all exhibit ferromagnetism, which suppresses superconductivity. Therefore, these structures are not considered in the subsequent analysis.

For these doped structures, we calculate their superconductivity as summarized in Table. Several doped structures show varying degrees of improvement compared to the original phase's T_c. T_c of $RbTi_3Bi_4Sn$ and $RbTi_3Bi_4Pb$ belonging to hole doping can be raised to around 3 K. However, when increasing the doping concentration to 40% for Sn and Pb doping, denoted as $RbTi_3BiSn_2$ and $RbTi_3Bi_3Pb_2$, the results indicate that there is no obvious increase in T_c's. The electronic bands and DOS of these doped structures are given in Figs. S9 to S24. The kagome VHSs and flat band originating from Ti in-plane orbitals in the band structures are prominent, which undergo dramatic changes upon Ti doping but relatively maintain structural characteristics in the cases of Bi doping. As examples of hole and electron doping, respectively, the electronic energy bands and DOS of $RbTi_3Bi_4Sn$ and $RbTi_3Bi_4Te$ are plotted in Fig. 5B and C. The kagome flat band of $RbTi_3Bi_4Sn$ and the VHSs of $RbTi_3Bi_4Te$ are shifted close to the Fermi level, and the DOS originating from the flat band and VHSs exhibit pronounced peaks near the Fermi level. This indicates a shift of the Fermi level while maintaining the character of kagome band structures. These results are consistent with the above rigid band model, demonstrating that both electron and hole doping can improve T_c by tuning the kagome electronic structures and increasing the DOS through doping. The effective modulation of superconducting properties and kagome electronic structures by doping highlights the need for further experimental investigations in this system.

Discussion

The two superconducting domes observed in AV_3Sb_5 at low pressures are commonly believed to be related to the competition of CDW phases [30,32,36]. However, theoretical analyses of the superconducting dome at around 20 to 40 GPa are limited [65,68,69]. The properties of $CsTi_3Bi_5$ and AV_3Sb_5 at high pressure, in the absence of CDW, are similar, suggesting that our explanations for the superconducting dome and valley in $CsTi_3Bi_5$ may also apply to AV_3Sb_5. Recent research attributes the appearance of high-pressure superconducting dome in AV_3Sb_5 to transitions from hexagonal to monoclinic structures [70]. In contrast, our work demonstrates that the appearance of a similar dome in $CsTi_3Bi_5$ does not rely on structural phase transitions but rather originates from the transition from quasi-2D to 3D compression. Further investigations are needed to explore the similarities and differences in the superconducting properties of ATi_3Bi_5 and AV_3Sb_5 under pressure.

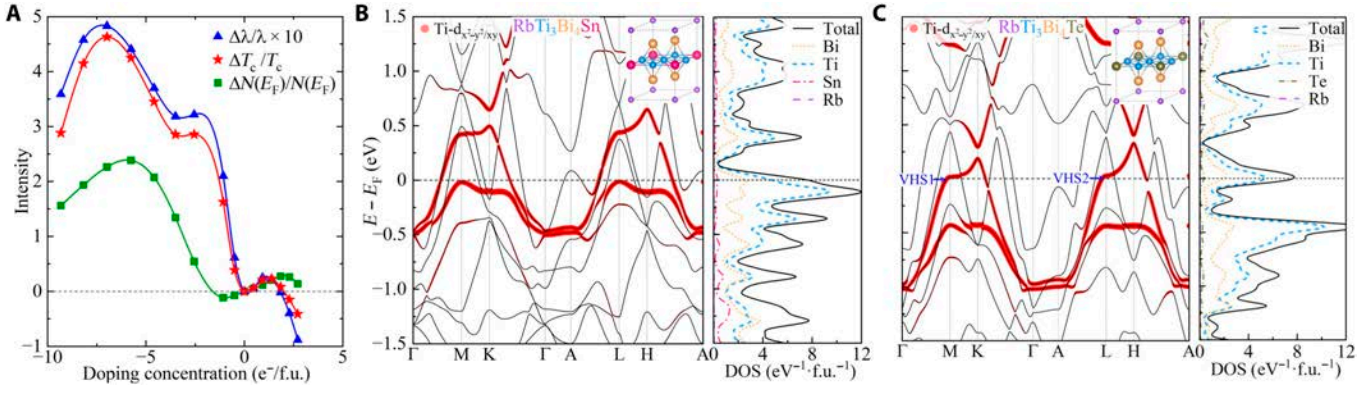


Fig. 5. Superconductivity and electronic structures of $RbTi_3Bi_5$ under doping. (A) Relative changes of λ, T_c, and $N(E_F)$ under doping using the rigid band model: $\Delta\lambda/\lambda$, $\Delta T_c/T_c$, and $\Delta N(E_F)/N(E_F)$. Calculated electronic band structures projected by Ti-$d_{x2-y2/xy}$ orbitals and partial DOS with SOC for (B) $RbTi_3Bi_4Sn$ and (C) $RbTi_3Bi_4Te$, where the insets show the doped structures. Two kagome VHSs near the Fermi level of $RbTi_3Bi_4Te$ are labeled as "VHS1" and "VHS2", respectively.

Table. Superconductivity of doped structures for $RbTi_3Bi_5$. EPC $\lambda(\omega = \infty)$, logarithmic average frequency ω_{log} (K), and T_c of doped structures.

	$RbTi_3Bi_5$	$RbVTi_2Bi_5$	$RbZrTi_2Bi_5$	$RbNbTi_2Bi_5$	$RbTi_3Bi_4Te$	$RbTi_3Bi_4Sb$	$RbTi_3Bi_4Sn$	$RbTi_3Bi_4Pb$	$RbTi_3Bi_3Sn_2$	$RbTi_3Bi_3Pb_2$
λ	0.520	0.578	0.525	0.586	0.526	0.513	0.605	0.608	0.612	0.622
ω_{log}(K)	135.8	131.3	113.7	126.5	137.7	144.9	124.6	117.8	127.6	119.1
T_c(K)	1.92	2.67	2.49	2.69	2.04	1.94	2.92	2.81	3.09	3.03

Exploring the possible phase transitions associated with structure or electronic orders in CsV_3Sb_5 is an intriguing topic [30,32,36,70]. Phonon spectra of ATi_3Bi_5 without imaginary frequencies in the pressure of 0 to 50 GPa in Fig. 3D to F and Figs. S3 and S5B show good dynamic stability, excluding the possibility of structural phase transition under pressure, however, an electronic nematic phase of $CsTi_3Bi_5$ at ambient pressure has been experimentally observed [51,53]. This nematic phase may be suppressed and eventually disappears under pressure, similar to the behaviors of CsV_3Sb_5 in experiment [32]. Consequently, there may be a possible nematic phase transition under pressure, which deserves further experimental study.

It should be noted that while λ_{Ti} contributes approximately 35% to the total EPC λ as shown in Fig. S6A, the electronic states near the Fermi level are primarily dominated by the kagome Ti atoms, as illustrated in Fig. 1B. Calculated electronic DOS projected on different atoms for $CsTi_3Bi_5$ in Fig. S2 indicate that about 64% of the DOS at the Fermi level come from Ti orbitals. In addition, tuning the Fermi level through hole doping can dramatically enhance superconductivity, mainly due to the enhancement of the DOS of Ti atoms as discussed in Superconductivity of $RbTi_3Bi_5$ Under Doping. Therefore, kagome lattice composed by Ti atoms plays a crucial role to the superconductivity.

Fu and Kane [71] proposed that the proximity effect between the helical Dirac TSS of a topological insulator and an s-wave superconductor can induce Majorana zero modes, which can be utilized for topological quantum calculations. This effect has been achieved in CsV_3Sb_5 [48]. Based on our calculations, pressure effectively induces abundant Dirac TSS near the Fermi level, whose combination with superconductivity theoretically gives rise to Majorana zero modes. This opens up another fascinating research topic for ATi_3Bi_5 and its potential for exploring topological quantum phenomena.

The interlayer van der Waals forces present in ATi_3Bi_5 facilitate their mechanical exfoliation from the bulk structures. We explore the structural stability and superconducting properties of $CsTi_3Bi_5$ in the 2D monolayer limit. Three slab structures, namely, $CsTi_3Bi_5$ (slab1), Ti_3Bi_5 (slab2), and $Cs_2Ti_3Bi_5$ (slab3), with different combinations of Ti_3Bi_5 layer and Cs layer are considered as seen in Fig. S25. Phonon calculations show that slab2 has minimal imaginary frequencies, while slab1 and slab3 display good dynamic stability. However, superconducting calculations reveal that their T_c's are nearly equal to that of the bulk structures.

Conclusion

In summary, we preemptively analyze superconducting and topological properties under pressure and doping for ATi_3Bi_5, as well as their thermal conductivity, heat capacity, electrical resistance, and SHC using first-principles calculations. The estimated T_c of $CsTi_3Bi_5$ presents a special down-up-down trend with increasing pressure. The two decreasing sections can be attributed to the decrease in EPC resulting from reduced electronic DOS and $\langle\omega^2\rangle$ with increasing pressure. Within this overall decreasing trend, the abnormally increased part is associated with the sharply enhanced EPC in the low-frequency region induced by vertical vibration modes, which is related to the transition from anisotropic to isotropic compression from a structural perspective. With rigid band model calculations under doping, T_c of $RbTi_3Bi_5$ can increase by nearly 5 times accompanied by increased electronic DOS and EPC. Calculations for different atomic substitution structures in $RbTi_3Bi_5$ show improvements of T_c from 1.9 to 3.1 K. Furthermore, doping and pressure serve as effective means to tune the kagome VHSs and flat band positions close to E_F. Pressure can also induce abundant Dirac-type TSS at E_F. Additionally, our transport calculations agree well with recent experimental results, indicating the absence of CDW. The resistance of $CsTi_3Bi_5$ shows normal metal behavior, and its thermal transport is predominantly governed by electronic contributions. The SHC of $CsTi_3Bi_5$ can reach up to $226\hbar \cdot(e\cdot \Omega \cdot cm)^{-1}$ near the Fermi level. Our comprehensive analysis of the diverse physical properties in ATi_3Bi_5 underscores the need for further experimental exploration in this field.

Methods

The methods can be found in the Supplementary Materials.

Acknowledgments

Funding: This work is supported in part by the National Key R&D Program of China (Grant No. 2018YFA0305800), the Strategic Priority Research Program of the Chinese Academy of Sciences (Grant No. XDB28000000), the National Natural Science Foundation of China (Grant No.11834014), and the Innovation Program for Quantum Science and Technology (No. 2021ZD0301800). B.G. is supported in part by the National Natural Science Foundation of China (Grant No. 12074378), the Chinese Academy of Sciences (Grant No. YSBR-030 and No. Y929013EA2), the Strategic Priority Research Program of Chinese Academy of Sciences (Grant No. XDB33000000), and the Beijing Natural Science Foundation (Grant No. Z190011).
Author contributions: J.-Y.Y., B.G., and G.S. designed and supervised the research. X.-W.Y. performed theoretical calculations. All authors participated in analyzing results. X.-W.Y., J.-Y.Y., B.G., and G.S. prepared the figures and manuscript.

Competing interests: The authors declare that there is no conflict of interest regarding the publication of this article.

Data Availability

The data that support the findings of this study are available from the corresponding authors upon reasonable request.

Supplementary Materials

Methods
Figs. S1 to S25
Tables S1 and S2
References [72–80]

References

1. Syozi I statistics of kagome lattice. *Prog Theor Phys*. 1951;6(3):306–308.
2. Yin JX, Lian B, Hasan MZ. Topological kagome magnets and superconductors. *Nature*. 2022;612(7941):647–657.
3. Yin JX, Zhang SS, Chang G, Wang Q, Tsirkin SS, Guguchia Z, Lian B, Zhou H, Jiang K, Belopolski I, et al. Negative flat band magnetism in a spin-orbit-coupled correlated kagome magnet. *Nat Phys*. 2019;15(5):443–448.
4. Gong SS, Zhu W, Sheng DN. Emergent chiral spin liquid: Fractional quantum Hall effect in a kagome heisenberg model. *Sci Rep*. 2014;4(1):6317.
5. Tang E, Mei JW, Wen XG. High-temperature fractional quantum Hall states. *Phys Rev Lett*. 2011;106(23):236802.
6. Jiang HC, Devereaux T, Kivelson SA. Wigner crystal in a lightly doped kagome quantum spin liquid. *Phys Rev Lett*. 2017;119(6):067002.
7. Miyahara S, Kusuta S, Furukawa N. BCS theory on a flat band lattice. *Phys C: Superconduct*. 2007;460-462:1145.
8. Ohgushi K, Murakami S, Nagaosa N. Spin anisotropy and quantum Hall effect in the kagome lattice: Chiral spin state based on a ferromagnet. *Phys Rev B*. 2000;62(10):R6065.
9. Guo HM, Franz M. Topological insulator on the kagome lattice. *Phys Rev B*. 2009;80(11):113102.
10. Kiesel ML, Platt C, Thomale R. Unconventional Fermi surface instabilities in the kagome Hubbard model. *Phys Rev Lett*. 2013;110(12):126405.
11. Kiesel ML, Thomale R. Sublattice interference in the kagome Hubbard model. *Phys Rev B*. 2012;86(12):121105.
12. Wang WS, Li ZZ, Xiang YY, Wang QH. Competing electronic orders on kagome lattices at van Hove filling. *Phys Rev B*. 2013;87(11):115135.
13. Liu DF, Liang AJ, Liu EK, Xu QN, Li YW, Chen C, Pei D, Shi WJ, Mo SK, Dudin P, et al. Magnetic Weyl semimetal phase in a kagome crystal. *Science*. 2019; 365(6459):1282–1285.
14. Morali N, Batabyal R, Nag PK, Liu E, Xu Q, Sun Y, Yan B, Felser C, Avraham N, Beidenkopf H. Fermi-arc diversity on surface terminations of the magnetic Weyl semimetal $Co_3Sn_2S_2$. *Science*. 2019;365(6459):1286–1291.
15. You JY, Feng YP. A two-dimensional kagome magnet with tunable topological phases. *Mater Today Chem*. 2023;30:101566.
16. Liu E, Sun Y, Kumar N, Muechler L, Sun A, Jiao L, Yang SY, Liu D, Liang A, Xu Q, et al. Giant anomalous Hall effect in a ferromagnetic kagome-lattice semimetal. *Nat Phys*. 2018;14(11):1125.
17. Nayak AK, Fischer JE, Sun Y, Yan B, Karel J, Komarek AC, Shekhar C, Kumar N, Schnelle W, Kübler J, et al. Large anomalous Hall effect driven by a nonvanishing berry curvature in the noncolinear antiferromagnet Mn_3Ge. *Sci Adv*. 2016;2(4):e1501870.
18. Nakatsuji S, Kiyohara N, Higo T. Large anomalous hall effect in a non-collinear antiferromagnet at room temperature. *Nature*. 2015;527(7577):212.
19. Xu G, Lian B, Zhang SC. Intrinsic quantum anomalous Hall effect in the kagome lattice $Cs_2LiMn_3F_{12}$. *Phys Rev Lett*. 2015;115(18):186802.
20. Zhang Z, You JY, Ma XY, Gu B, Su G. Kagome quantum anomalous Hall effect with high chern number and large band gap. *Phys Rev B*. 2021;103(1):014410.
21. Baidya S, Mallik AV, Bhattacharjee S, Saha-Dasgupta T. Interplay of magnetism and topological superconductivity in bilayer kagome metals. *Phys Rev Lett*. 2020;125(2):026401.
22. You JY, Gu B, Su G, Feng YP. Emergent kagome electrides. *J Am Chem Soc*. 2022;144(12):5527.
23. Ortiz BR, Gomes LC, Morey JR, Winiarski M, Bordelon M, Mangum JS, Oswald IWH, Rodriguez-Rivera JA, Neilson JR, Wilson SD, et al. New kagome prototype materials: Discovery of KV_3Sb_5, RbV_3Sb_5, and CsV_3Sb_5. *Phys Rev Mater*. 2019;3(9):094407.
24. Ortiz BR, Sarte PM, Kenney EM, Graf MJ, Teicher SML, Seshadri R, Wilson SD. Superconductivity in the Z_2 kagome metal KV_3Sb_5. *Phys Rev Mater*. 2021;5(3):034801.
25. Ortiz BR, Teicher SML, Hu Y, Zuo JL, Sarte PM, Schueller EC, Abeykoon AMM, Krogstad MJ, Rosenkranz S, Osborn R, et al. CsV_3Sb_5: A Z_2 topological kagome metal with a superconducting ground state. *Phys Rev Lett*. 2020;125(24):247002.
26. Yin Q, Tu Z, Gong C, Fu Y, Yan S, Lei H. Superconductivity and normal-state properties of kagome metal RbV_3Sb_5 single crystals. *Chin Phys Lett*. 2021;38(3):037403.
27. Chen H, Yang H, Hu B, Zhao Z, Yuan J, Xing Y, Qian G, Huang Z, Li G, Ye Y, et al. Roton pair density wave in a strong-coupling kagome superconductor. *Nature*. 2021; 599(7884):222.
28. Du F, Luo S, Ortiz BR, Chen Y, Duan W, Lu X, Wilson SD, Song Y, Yuan H. Pressure-induced double superconducting domes and charge instability in the kagome metal KV_3Sb_5. *Phys Rev B*. 2021;103(22):L220504.
29. Li H, Zhang TT, Yilmaz T, Pai YY, Marvinney CE, Said A, Yin QW, Gong CS, Tu ZJ, Vescovo E, et al. Observation of unconventional charge density wave without acoustic phonon anomaly in kagome superconductors AV_3Sb_5 (A=*Rb*, *Cs*). *Phys Rev X*. 2021;11(3):031050.
30. Chen KY, Wang NN, Yin QW, Gu YH, Jiang K, Tu ZJ, Gong CS, Uwatoko Y, Sun JP, Lei HC, et al. Double superconducting dome and triple enhancement of T_c in the kagome superconductor CsV_3Sb_5 under high pressure. *Phys Rev Lett*. 2021;126(24):247001.
31. Nie L, Sun K, Ma W, Song D, Zheng L, Liang Z, Wu P, Yu F, Li J, Shan M, et al. Charge-density-wave-driven electronic nematicity in a kagome superconductor. *Nature*. 2022;604(6904):59–64.
32. Zheng L, Wu Z, Yang Y, Nie L, Shan M, Sun K, Song D, Yu F, Li J, Zhao D, et al. Emergent charge order in pressurized kagome superconductor CsV_3Sb_5. *Nature*. 2022;611(7937):682–687.
33. Zhao H, Li H, Ortiz BR, Teicher SML, Park T, Ye M, Wang Z, Balents L, Wilson SD, Zeljkovic I. Cascade of correlated

electron states in the kagome superconductor CsV_3Sb_5. *Nature*. 2021;599(7884):216–221.
34. Yin JX. Quantum dephasing of kagome superconductivity. *Sci Bull*. 2023;68(6):568–570.
35. Zhu CC, Yang XF, Xia W, Yin QW, Wang LS, Zhao CC, Dai DZ, Tu CP, Song BQ, Tao ZC, et al. Double-dome superconductivity under pressure in the V-based kagome metals AV_3Sb_5 (A=Rb and K). *Phys Rev B*. 2022;105(9):094507.
36. Yu FH, Ma DH, Zhuo WZ, Liu SQ, Wen XK, Lei B, Ying JJ, Chen XH. Unusual competition of superconductivity and charge-density-wave state in a compressed topological kagome metal. *Nat Commun*. 2021;12:3645.
37. Zhong Y, Liu J, Wu X, Guguchia Z, Yin JX, Mine A, Li Y, Najafzadeh S, das D, Mielke C III, et al. Nodeless electron pairing in CsV_3Sb_5-derived kagome superconductors. *Nature*. 2023;617(7961):488–492.
38. Ding G, Wo H, Gu Y, Gu Y, Zhao J. Effect of chromium doping on superconductivity and charge density wave order in the kagome metal $Cs(V_{1-x}Cr_x)_3Sb_5$. *Phys Rev B*. 2022;106(23):235151.
39. Liu Y, Wang Y, Cai Y. Doping evolution of superconductivity, charge order and band topology in hole-doped topological kagome superconductors $Cs(V_{1-x}Ti_x)_3Sb_5$. arXiv. 2021. https://doi.org/10.48550/arXiv.2110.12651
40. Wu P, Tu YB, Wang ZY, Yu S, Li H, Ma W, Liang Z, Zhang Y, Zhang X, Li Z, et al. Unidirectional electron-phonon coupling in the nematic state of a kagome superconductor. *Nat Phys*. 2023;19(8):1143.
41. Yang H, Huang Z, Zhang Y. Titanium doped kagome superconductor $CsV_{3-x}Ti_xSb_5$ and two distinct phases. *Sci Bull*. 2022;67:2176-2185.
42. Oey YM, Ortiz BR, Kaboudvand F. Fermi level tuning and double-dome superconductivity in the kagome metal $CsV_3Sb_{5-x}Sn_x$. *Phys Rev Mater*. 2022;6(4):L041801.
43. Oey YM, Kaboudvand F, Ortiz BR, Seshadri R, Wilson SD. Tuning charge density wave order and superconductivity in the kagome metals $KV_3Sb_{5-x}Sn_x$ and $RbV_3Sb_{5-x}Sn_x$. *Phys Rev Mater*. 2022;6(7):Article 074802.
44. Liu M, Han T, Hu X. Evolution of superconductivity and charge density wave through Ta and Mo doping in CsV_3Sb_5. *Phys Rev B*. 106(14):L140501.
45. Liu Y, Liu CC, Zhu QQ, Ji LW, Wu SQ, Sun YL, Bao JK, Jiao WH, Xu XF, Ren Z, et al. Enhancement of superconductivity and suppression of charge-density wave in As-doped CsV_3Sb_5. *Phys Rev Mater*. 2022;6(12):124803.
46. Zhou X, Li Y, Liu Z, Hao J, Dai Y, Wang Z, Yao Y, Wen HH. Effects of niobium doping on the charge density wave and electronic correlations in the kagome metal $Cs(V_{1-x}Nb_x)_3Sb_5$. *Phys Rev B*. 2023;107(12):125124.
47. Hu Y, Teicher SML, Ortiz BR. Topological surface states and flat bands in the kagome superconductor $CsV_3Sb_{5-x}Sn_x$. *Sci Bull*. 2022;67:495.
48. Liang Z, Hou X, Zhang F. Three-dimensional charge density wave and surface-dependent vortex-core states in a kagome superconductor CsV_3Sb_5. *Phys Rev X*. 2021;11(5):031026.
49. Yi XW, Ma XY, Zhang Z, Liao ZW, You JY, Su G. Large kagome family candidates with topological superconductivity and charge density waves. *Phys Rev B*. 2022;106(22):L220505.
50. Yang H, Zhao Z, Yi XW. Titanium-based kagome superconductor $CsTi_3Bi_5$ and topological states. arXiv. 2022. https://doi.org/10.48550/arXiv.2209.03840
51. Yang H, Ye Y, Zhao Z. Superconductivity and orbital-selective nematic order in a new titanium-based kagome metal $CsTi_3Bi_5$. arXiv. 2022. https://doi.org/10.48550/arXiv.2211.12264
52. Werhahn D, Ortiz BR, Hay AK, Wilson SD, Seshadri R, Johrendt D. The kagomé metals $RbTi_3Bi_5$ and $CsTi_3Bi_5$. *Zeitschrift für Naturforschung B*. 2022;77(11-12):757–764.
53. Li H, Cheng S, Ortiz BR, Tan H, Werhahn D, Zeng K, Johrendt D, Yan B, Wang Z, Wilson SD, et al. Electronic nematicity without charge density waves in titanium-based kagome metal. *Nat. Phys.* 2023. https://doi.org/10.1038/s41567-023-02176-3
54. Yi XW, Liao ZW, You JY, Gu B, Su G. Topological superconductivity and large spin Hall effect in the kagome family Ti_6X_4 (X = bi, Sb, Pb Tl, and In). *iScience*. 2023;26(1):105813.
55. Chen X, Liu X, Xia W, Mi X, Zhong L, Yang K, Zhang L, Gan Y, Liu Y, Wang G, et al. Electrical and thermal transport properties of the kagome metals ATi_3Bi_5 (A=Rb,Cs). *Phys Rev B*. 2023;107(17):174510.
56. Yang J, Yi X, Zhao Z, Xie Y, Miao T, Luo H, Chen H, Liang B, Zhu W, Ye Y, et al. Observation of flat band, dirac nodal lines and topological surface states in kagome superconductor $CsTi_3Bi_5$. *Nat Commun*. 2023;14(1):4089.
57. Hu Y, Le C, Zhao Z. Non-trivial band topology and orbital-selective electronic nematicity in a new titanium-based kagome superconductor. arXiv. 2022. https://doi.org/10.48550/arXiv.2212.07958
58. Jiang Z, Liu Z, Ma H, Xia W, Liu Z, Liu J, Cho S, Yang Y, Ding J, Liu J, et al. Flat bands, non-trivial band topology and electronic nematicity in layered kagome-lattice $RbTi_3Bi_5$. arXiv. 2022. https://doi.org/10.48550/arXiv.2212.02399
59. Zhou Y, Chen L, Ji X. Physical properties, electronic structure, and strain-tuned monolayer of the weak topological insulator $RbTi_3Bi_5$ with kagome lattice. arXiv. 2023. https://doi.org/10.48550/arXiv.2301.01633
60. Liu B, Kuang MQ, Luo Y, Li Y, Hu C, Liu J, Xiao Q, Zheng X, Huai L, Peng S, et al. Tunable van Hove singularity without structural instability in kagome metal $CsTi_3Bi_5$. *Phys Rev Lett*. 2023;131(2):026701.
61. Wang Y, Liu Y, Hao Z, Cheng W, Deng J, Wang Y, Gu Y, Ma XM, Rong H, Zhang F, et al. Flat band and Z_2 topology of kagome metal $CsTi_3Bi_5$. *Chin Phys Lett*. 2023;40(3):037102.
62. You JY, Su G, Feng YP. A versatile model with three-dimensional triangular lattice for unconventional transport and various topological effects. *Nat Sci Rev*. 2023;nwad114.
63. Zhang JF, Liu K, Lu ZY. First-principles study of the double-dome superconductivity in the kagome material CsV_3Sb_5 under pressure. *Phys Rev B*. 2021;104(19):195130.
64. Si J, Lu W, Sun Y, Liu P, Wang B. Charge density wave and pressure-dependent superconductivity in the kagome metal CsV_3Sb_5: A first-principles study. *Phys Rev B*. 2022;105(2):024517.
65. Zhang Z, Chen Z, Zhou Y, Yuan Y, Wang S, Wang J, Yang H, An C, Zhang L, Zhu X, et al. Pressure-induced reemergence of superconductivity in the topological kagome metal CsV_3Sb_5. *Phys Rev B*. 2021;103(22):224513.
66. McMillan WL. Transition temperature of strong-coupled superconductors. *Phys Rev*. 1968;167(2):331.
67. Allen PB, Dynes RC. Transition temperature of strong-coupled superconductors reanalyzed. *Phys Rev B*. 1975;12(3):905.

68. Tsirlin A, Fertey P, Ortiz BR, Klis B, Merkl V, Dressel M, Wilson S, Uykur E. Role of Sb in the superconducting kagome metal CsV_3Sb_5 revealed by its anisotropic compression. *SciPost Physics*. 2022;12(2):49.
69. Yu F, Zhu X, Wen X, Gui Z, Li Z, Han Y, Wu T, Wang Z, Xiang Z, Qiao Z, et al. Pressure-induced dimensional crossover in a kagome superconductor. *Phys Rev Lett*. 2022;128(7):077001.
70. Du F, Li R, Luo S. Superconductivity modulated by structural phase transitions in pressurized vanadium-based kagome metals. *Phys Rev B*. 2022;106(2):024516.
71. Fu L, Kane CL. Superconducting proximity effect and Majorana fermions at the surface of a topological insulator. *Phys Rev Lett*. 2008;100(9):096407.
72. Kresse G, Furthmuller J. Efficient iterative schemes for ab initio total-energy calculations using a plane-wave basis set. *Phys Rev B Condens Matter*. 1996;54(16):11169–86.
73. Giannozzi P, Baroni S, Bonini N, Calandra M, Car R, Cavazzoni C, Ceresoli D, Chiarotti GL, Cococcioni M, Dabo I, et al. QUANTUM ESPRESSO: A modular and open-source software project for quantum simulations of materials. *J Phys Condens Matter*. 2009;21(39):395502.
74. Mostofi AA, Yates JR, Pizzi G, Lee YS, Souza I, Vanderbilt D, Marzari N. An updated version of wannier90: A tool for obtaining maximally-localised wannier functions. *Comput Phys Commun*. 2014;185:2309–2310.
75. Guo GY, Yao Y, Niu Q. Ab initio calculation of the intrinsic spin Hall effect in semiconductors. *Phys Rev Lett*. 2005;94(22):226601.
76. Sinova J, Culcer D, Niu Q, Sinitsyn NA, Jungwirth T, MacDonald AH. Universal intrinsic spin Hall effect. *Phys Rev Lett*. 2004;92(12):126603.
77. Wu Q, Zhang S, Song HF, Troyer M, Soluyanov AA. Wanniertools An open-source software package for novel topological materials. *Comput Phys Commun*. 2018;224(5806):405–416.
78. Madsen GKH, Singh DJ. Boltztrap. A code for calculating band-structure dependent quantities. *Comput Phys Commun*. 2006;175(1):67–71.
79. Togo A, Tanaka I. First principles phonon calculations in materials science. *Scr Mater*. 2015;108:1–5.
80. Poncé S, Margine ER, Verdi C, Giustino F. EPW: Electron-phonon coupling, transport and superconducting properties using maximally localized wannier functions. *Comput Phys Commun*. 2016;209:116–133.